

## 2. TOKAMAK ISTTOK

J.A.C. Cabral and C.A.F. Varandas (Heads), M.P. Alonso, B.B. Carvalho, H. Fernandes, H. Figueiredo, R. Gomes, I. Nedzelskij, V. Plyusnin, C. Silva, A. Soares, Y. Tashev

### 2.1. INTRODUCTION

The tokamak ISTTOK was in operation during about 35 weeks in 2001. The research and development (R&D) activities have been mainly centered in the following topics:

- Discharge production systems;
- Diagnostics;
- Plasma Physics studies.

### 2.2. DISCHARGE PRODUCTION SYSTEMS

#### 2.2.1. Introduction

The following main tasks were carried out:

- Repair of the slow control system based on a commercial vacuum controller unit;
- Development of a new slow control system;
- Collaboration with the University of Riga on the preparation of a proposal for request of preferential support concerning the testing on ISTTOK of the liquid metal limiter concept.

#### 2.2.2. New slow control system

A new slow control system has been developed for the replacement of the existing system based on a ten years old commercial vacuum controller. This system monitors the operation of the vacuum pumping and measuring units, the discharge cleaning system, the condenser banks, the gas injection units, the safety systems and the power supplies for the toroidal magnetic field and pre-magnetization of the transformer iron core.

This new slow control system (Figure 2.1) is based on a Personnel Computer (Pentium III, 750 MHz, 256 kb RAM and 40 Gb hard disk) connected by RS232 to a commercial vacuum controller unit and by CANbus (ISO 11898) to several Eurocard 3U crates, which house the following on-site developed modules with:

- Eight optical fiber digital outputs;
- Eight optical fiber inputs;
- Eight solid-state relays (LCA 110) with 200 mA maximum current;

- Eight galvanic isolated and multiplexed digitizer channels, with 10 bits resolution, programmable sampling rate up to 1 kSPS and programmable gain;
- Two galvanic isolated channels with 10 bit resolution, PWM based digital-to-analogue conversion and programmable gain.

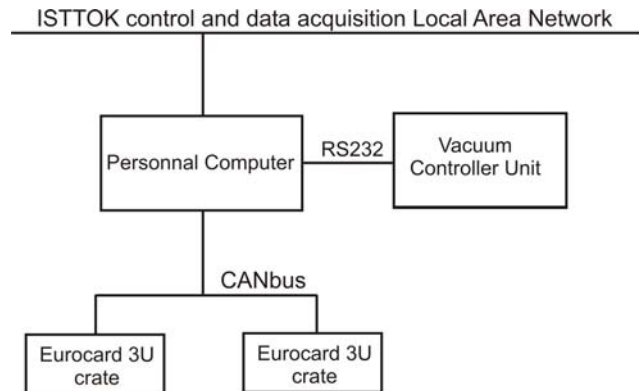


Figure 2.1 – Block diagram of the new slow control system

#### 2.2.3. Testing of the liquid metal limiter concept

An important issue in magnetic fusion research is the power exhaust under steady state operation conditions and during transient events like, for instance, ELMS and disruptions. The high power loads (up to 100 MW/m<sup>2</sup>) may be responsible for reducing the lifetime of the plasma facing component (PFC).

To ensure reduced erosion and stresses, usually present in solid surfaces, while providing an efficient mean to exhaust heat produced in the core plasma, it was proposed to use liquid metals (LM) flows in the interface of the two media. Due to their specific thermal properties, liquid metals are suitable materials to achieve that goal.

Experiments on liquid metals were made on the soviet tokamak T3-M in the eighties and presently in two American facilities: DIII-D (in San Diego) and CDX-U (in Princeton).

The EURATOM Fusion Programme has not carried out until now any specific programme concerning the testing of the use of liquid metals on fusion experiments. Since the implementation of LM divertor or wall in large fusion devices requires tests on smaller scale machines, the Portuguese and Latvian EURATOM Associations have decided to establish a joint R&D programme aiming at testing the LM limiter concept on ISTTOK. The Consultative Committee of the EURATOM Fusion Programme approved on February 1<sup>st</sup> 2002 this programme for preferential support.

This R&D programme has the following main objectives:

- To analyse the dynamic behaviour of liquid metal jets in magnetic fields;
- To study jet-plasma behaviour in a magnetic field and the dependence of the results on liquid metal parameters (like, for instance, temperature and flow velocity);
- To verify the feasibility of ISTTOK operation with a liquid metal limiter;
- To study the influence of the liquid metal limiter on the main plasma parameters ( $I_p$ ,  $T_e$ ,  $N_e$ ) as well as on the plasma stability and confinement;
- To study the influence of the LM limiter radial position on the plasma parameters;
- To measure the heat deposited on the LM jet by IR or other (thermocouple) procedures;
- To analyse the overall plasma impurity content as well as the Ga radial profiles using passive and active spectroscopic diagnostic;
- To study the influence of liquid metal limiter biasing on the plasma confinement and stability.

## 2.3. DIAGNOSTICS

### 2.3.1. Introduction

The following main activities were performed:

- Installation and operation of a new injector of the heavy ion beam diagnostic;
- Development of a sweeper generator for the triple emissive probe;
- Study of the influence of a non-uniform B-field on the measurement of the  $n_e\sigma_{\text{eff}}$  profile by heavy ion beam probing with a multiple cell array detector;

- Development of a power supply to drive the hollow cathode spectral lamp of a new visible spectrometer;
- Design and construction of trigger modules, for synchronisation with the tokamak discharges, of the detection camera of the visible spectrometer (both OMA and image intensifier are triggered);
- Installation and alignment of the visible spectrometer in order to have  $C^{III}$  line monitoring the relative plasma density as well as the ion temperature. Both spectrometers are installed in parallel;
- Development of a real-time MHD diagnostic for feedback control of the ISTTOK operation.

### 2.3.2. New injector of the heavy ion beam diagnostic

This new injector with a thermo-ionic ion source permits to obtain inside the tokamak vessel  $Cs^+$  beams with currents up to 7  $\mu A$  and a diameter of 2 mm. Therefore the new injector allows to increase the intensity of the secondary beam and to start the mastering of time-of-flight measurements with its secondary ions, leading to the measurement of the plasma potential radial profile.

### 2.3.3. Sweeper generator for the triple emissive probe

This sweeper (Figure 2.2) is constituted by a triangular wave oscillator, which output signal is power increased by an operational amplifier (TDA1521) typically used in the acoustic band. Afterwards the signal voltage is amplified ( $\pm 150$ ) by an 10:1 transformer.

### 2.3.4. Influence of a non-uniform B-field on the measurement of the $n_e\sigma_{\text{eff}}$ profile by heavy ion beam probing with a multiple cell array detector

The radial profile of the product  $n_e\sigma_{\text{eff}}$  can be directly obtained using a heavy ion beam diagnostic (HIBD) and measuring the currents of secondary ions ( $i_s$ ) created in collisions between the plasma electrons and the primary ions, and collected by a multiple cell array detector (MCAD).

For the double charged secondary ions the relation between  $i_s$  and  $n_e\sigma_{\text{eff}}$  is:

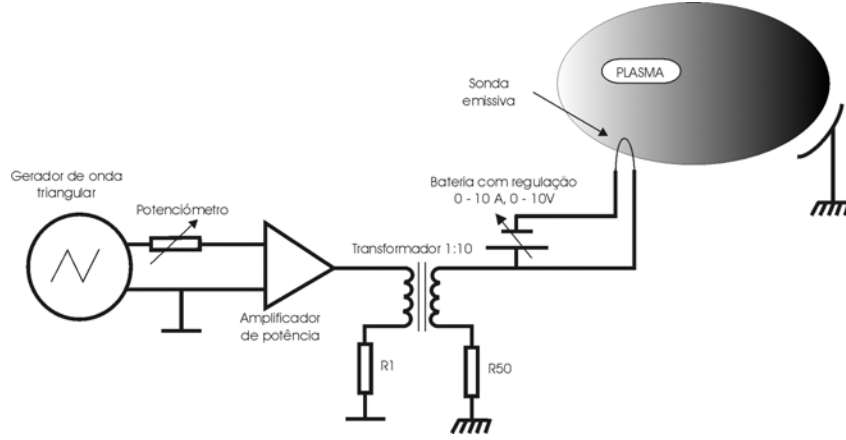


Figure 2.2 - Schematic of the sweeper circuit

$$i_s(r) = 2i_p[n_e \times \sigma_{\text{eff}}](r)\lambda(r)\xi(r) \quad (2.1)$$

where  $i_p$  is the intensity of the primary beam,  $\lambda(r)$  is the primary trajectory length (sample length) from which the secondary ions are collected by the cell and  $\xi(r)$  is the combined exponential beam attenuation coefficient.

In general, the signal from any cell of the MCAD is the sum of the secondary ion beam current and the currents due to secondary electrons created by the impact on the cell surface of both the beam particles and the plasma ultraviolet (UV) photons. Since the detector is usually located close to the vessel wall, the electron part of the current can be influenced by stray magnetic fields, resulting in suppression and/or exchange of the secondary electrons on the detector cells. Such an influence will have a non-homogeneous character, if the magnetic field is non-uniform across the MCAD. Obviously, the measured  $i_s$  profiles, in this case, will not be correct in what concerns equation (2.1).

The MCAD of the HIBD installation of the tokamak ISTTOK just satisfies the above mentioned conditions: it occupies a region between inner (cell #1) and outer (cell #12) radii of the toroidal coils, where the magnetic field decays from its nominal value to almost zero. The characteristic distribution of the background signals along the cells at a time  $t = 16$  ms of a discharge is shown in Figure 2.3 for shot #9315 ( $I_p \cong 9$  kA,  $\langle n_e \rangle \cong 4 \times 10^{18} \text{ m}^{-3}$ ,  $T_e \cong 180$  eV).

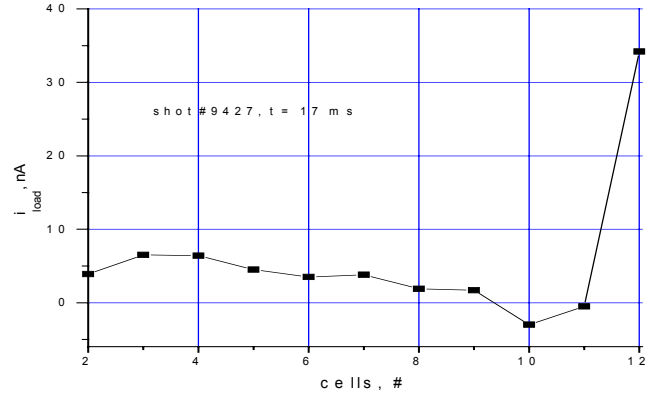


Figure 2.3 – Distribution of the background signal along the cells

A simple correction model has been developed based on the assumption that the UV flux from the plasma is distributed uniformly among the cells, and the postulate that the UV photo and ion beam secondary electrons are similarly influenced by the magnetic field. Then, the plasma background signal and the signal created by secondary ion beam from any  $k$ -cell can be respectively expressed by:

$$i_{\text{uve}(k)} = i_{\text{uv}} a_f (1 - b_{(k)}) \quad (2.2)$$

$$i_{b(k)} = i_{s(k)} + i_{se(k)} = i_{s(k)} [1 + a_b (1 - b_{(k)})] \quad (2.3)$$

where  $i_{\text{uv}}$  is the uniform UV flux,  $a_f$  is the effective photo-emission coefficient,  $b_{(k)}$  is the combined electron exchange-suppression coefficient, and  $a_b$  is the secondary electron emission coefficient.

Equation (2.2), with  $i_{uv}a_f = i_{uve(12)}$  ( $b_{(12)} = 0$ ), gives the coefficients  $b_{(k)}$  for any  $k$ -cell, while Equation (2.3), with a known coefficient  $a_b$ , allows to calculate  $i_{s(k)}$  and obtain the corrected profiles.

Figure 2.4 shows the raw and corrected  $i_s$  profiles obtained at  $t = 16$  ms on the same shot #9315. It is seen that corrections may attain substantial values and modify the shape of these profiles.

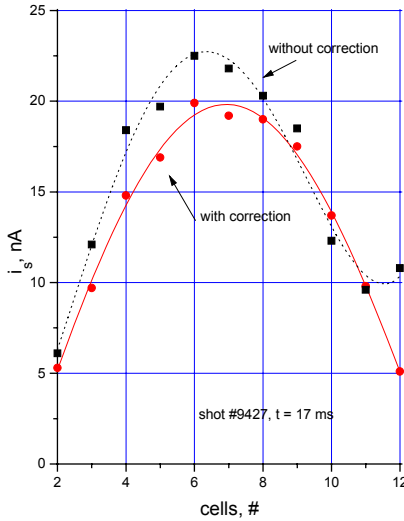


Figure 2.4 – the raw and the corrected  $n_e \sigma_{eff}$  profiles

### 2.3.5. Real-time MHD diagnostic for feedback control of the ISTTOK operation

A real-time MHD diagnostic is being developed aiming at:

- To monitor the characteristics of the plasma column during the tokamak discharges;
- To perform real-time feedback control of some operation parameters (primary voltage, vertical and horizontal magnetic fields and gas puffing).

This diagnostic is composed by twelve magnetic probes installed at a tokamak poloidal section and a new node of the ISTTOK distributed control and data acquisition system.

The pick-up coils, with a stop band of 1 MHz, have 50 windings over a  $42 \text{ mm}^2$  area and a length of 6mm (Figure 2.5). These coils are equally spaced ( $30^\circ$ ) on a poloidal plane of the tokamak, starting at  $6.5^\circ$  from the equator and at a central radius of 9,3 cm. The support is flexible, allowing their insertion through a normalized port of 6,8 cm (Figure. 2.5). After its

installation inside the ISTTOK vacuum chamber, the coil support gains the cylindrical configuration.

The new node of the ISTTOK control and data acquisition system is composed of:

- A Personnel Computer (PC) Pentium 4, 1.7 GHz, 512 Mb RAM and 40 Gb hard disk, running Windows 2000 as well as SQL database client and signal graphic display software;
- A Eurocard 3U crate housing:
  - (i) A Digital Signal Processor (DSP) board, based on a TI320C6711DSP running at 150 MHz providing 900 MFLOPS, with 16 Mb of 100 MHz synchronous dynamic random access memory. This board is connected to the PC by IEEE1284 parallel cable through the RTDX bi-directional communication protocol. This DSP runs software for control of the digitizer operation, data processing, generation of the feedback control signals and communication with the Personnel Computer;
  - (ii) A commercial fast CMOS, low-power, 12 bits digitizer board (TI THS1206), with four single-ended ( $\pm 1 \text{ V}$  range), sample-and-hold multiplexed channels, with programmable sampling rate up to 6 MSPS. This board was on-site improved to include an optical input trigger signal provided by the ISTTOK central timing system and an optical output providing a pulse width modulation signal for feedback control;
  - (iii) One on-site developed board with four multiplexers, each one with three inputs.
  - (iv) Two on-site developed galvanic isolation boards, each one with six channels based one ISO124 isolation amplifier;
  - (v) Three on-site developed analogue integration boards, each one with four channels with dynamic gain of 4 dB at 1 kHz. The on-site developed board is connected by a dedicated analogue backplane bus.

The signals from each probe are firstly integrated and galvanically isolated. Signals from each set of three probes are afterwards connected to a multiplexer, which is finally linked to one digitizer input (Figure 2.6).

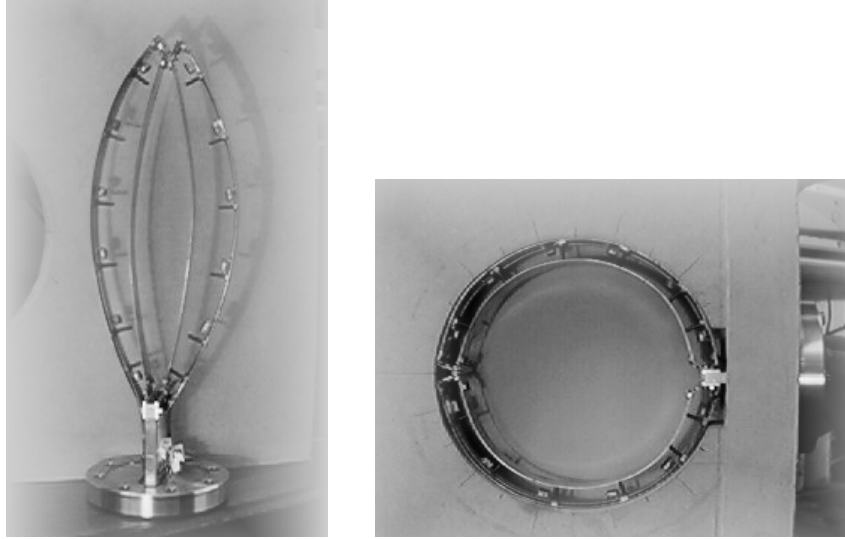


Figure 2.5 – Photographies of the set of coils and the flange support before and after assembly (simulated port)

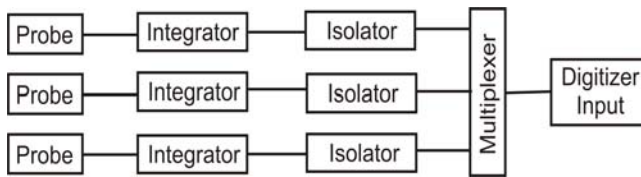


Figure 2.6 – Block diagram of each data acquisition channel

## 2.4. PLASMA PHYSICS STUDIES

### 2.4.1. Introduction

The following main experimental activities were performed:

- Influence of electrode and limiter biasing on the ISTTOK boundary plasma and on the main plasma confinement and stability;
- Measurements of plasma potential fluctuations in the edge region<sup>1</sup>;
- Transport modelling and numerical reconstruction of the runaway process.

### 2.4.2. Influence of electrode and limiter biasing on the ISTTOK boundary plasma and on the main plasma confinement and stability

#### 2.4.2.1. Introduction

Two different biasing scenarios have been studied on ISTTOK: Limiter bias (LB) and Electrode bias (EB), aiming at to compare their effects on the edge plasma

parameters and on the plasma confinement and stability. Both DC (from -300 V to + 300 V) and alternating (50 Hz, 80-130 p.V) bias voltages have been used. The latter has the advantage of not only allow the investigation of the effect of bias in a single shot, but also determine biasing thresholds for confinement modifications. The bias voltage is applied between the limiters/electrode and the vacuum vessel. In the experiments reported here, the electrode tip is situated at  $r=7$  cm, that is 1.5 cm inside the limiter.

Taking a typical ISTTOK discharge ( $I_p \sim 4-8$  kA,  $\tau_D \sim 30-40$  ms,  $n_e(0) \sim 5-10 \times 10^{18} \text{ m}^{-3}$ ,  $T_e(0) \sim 100-180$  eV,  $\tau_E \sim 0.5$  ms,  $\beta \sim 0.5$  %,  $q(0) \sim 1$ ,  $q(a) \sim 5$ ) as a reference, studies concerning the influence of limiter and electrode biasing on plasma confinement and stability have been carried out.

#### 2.4.2.2. Electrode

A movable electrode has been developed for biasing experiments on ISTTOK (Figure 2.7). The electrode head of this electrode is a mushroom shaped made of 2-D Carbon composite, screwed to a stainless steel shaft, that is protected by boron nitride as insulating material to be exposed to the plasma. The overall stroke length of the electrode is  $\approx 100$  mm ( $-50 < r_{\text{electrode-a}} < 50$  mm).

It has been observed that for  $r_{\text{electrode-a}} > 30$  mm the electrode does not become a limiter and is

<sup>1</sup> In collaboration with the Innsbruck University.

capable of sustaining the heat load from the discharges and the extra load connected with biasing.

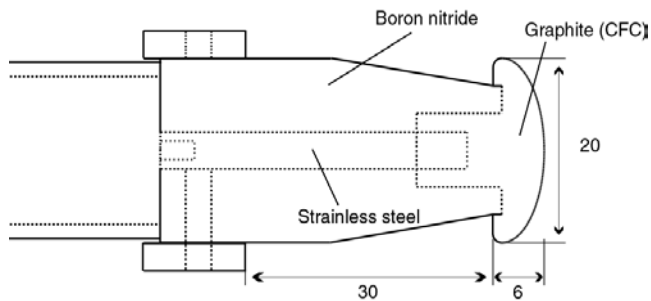


Figure 2.7 - Schematic illustration of the electrode head

#### 2.4.2.3. Limiter biasing

Limiter biasing experiments have been already described on the 2000 Annual Report. For positive bias, an increase (<30%) in the average plasma density ( $\langle n_e \rangle$ ) is observed, although, without a significant increase in the particle confinement. Analysis of a set of discharges has shown that (Figure 2.8) during the positive (negative) bias half-cycle, there is: (i) a decrease (increase) of the plasma current ( $I_p$ ), and of the electron temperature, ( $T_e$ ); and (ii) an increase (decrease) of the line averaged electron density ( $\langle n_e \rangle$ ) and of the intensity of the  $H_\alpha$  radiation.

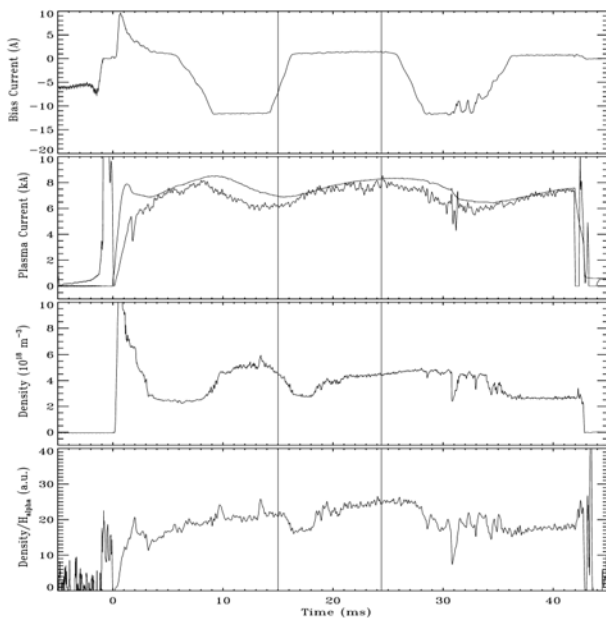


Figure 2.8 - Time evolution of the main plasma parameters for limiter biasing.

The transition from a negative biasing half-period to a positive one is made without significant loss of plasma confinement. On the contrary, the inverse transition (positive to negative biasing) impairs the discharge parameters, specially the plasma density, which drops considerably afterwards.

Changes in the global particle confinement time are inferred from the ratio of the line-averaged density to the  $H_\alpha$  line intensity. Although the average density increases for positive bias, the  $H_\alpha$  radiation also increases leading to very limited modifications in particle confinement. In spite of the lower density, particle confinement is larger for negative bias due to a low turbulent transport.

Analysis of the Langmuir probe data has shown that (Figure 2.9): (i) in the region around the limiter the edge plasma potential follows the applied voltage with the consequent change of  $E_r$  from  $\approx 3$  kV/m for positive bias to  $\approx 1$  kV/m for negative bias; and (ii)  $I_{sat}$  (a measure for the edge plasma density), inside the main plasma ( $r-a < -5$  mm), clearly increases (decreases) for positive (negative) bias. However, in the edge plasma ( $0 < r-a < 4$  mm),  $I_{sat}$  also increases for large negative voltages. This leads to a flatter edge density profile, in comparison with the more peaked ones obtained for positive biasing.

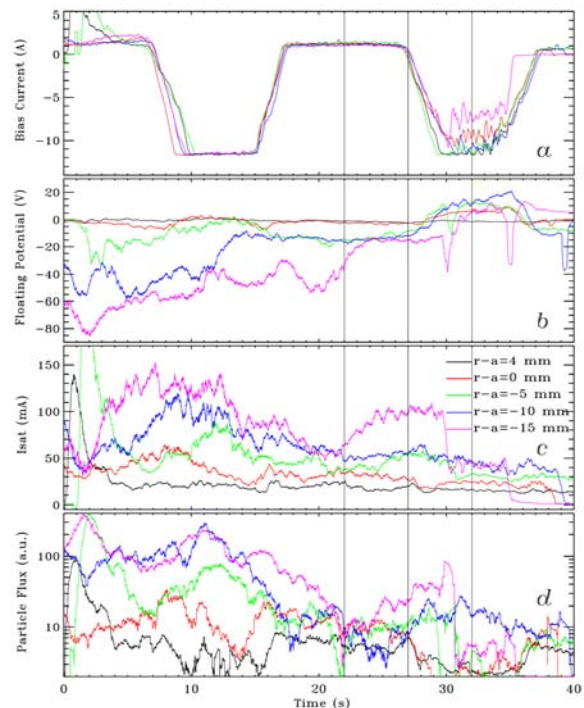


Figure 2.9 - Time evolution of the edge plasma parameters for a discharge with limiter bias

The Heavy ion Beam Diagnostic ( $X_e^+$  beam of 0.7  $\mu\text{A}$ , 22 keV) allows to observe gradual modifications on the  $n_e\sigma_{\text{eff}}$  profile (Figure 2.10). For the positive bias half cycle the plasma density increases leading to the peaking and to an upward shift ( $\sim 0.7$  cm) of the profile. For the negative bias half cycle changes in  $n_e$  are much smaller and the profile becomes flatter, regaining a more central position. In comparison with the reference (unbiased)  $n_e\sigma_{\text{eff}}$  profile, those obtained for either positive or negative bias show increased fluctuations levels.

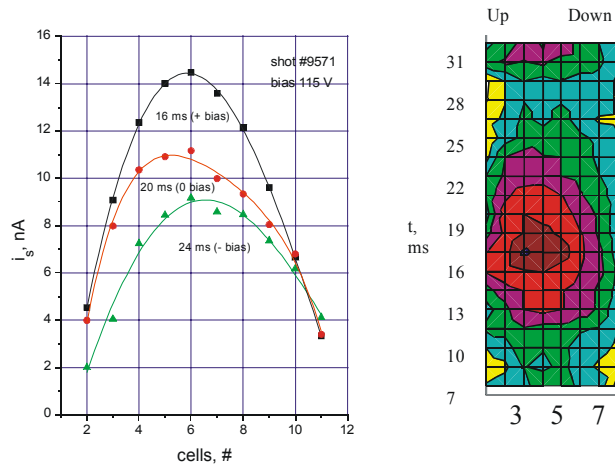


Figure 2.10 – Time evolution of the  $n_e\sigma_{\text{eff}}$  profile in shot #9571

The turbulent particle transport,

$$\Gamma_{ExB} = \langle \tilde{n} \tilde{E}_\theta \rangle / B$$

has been also computed from the probe data. The behavior of the cross-field particle flux, during biasing, is similar to that of  $I_{\text{sat}}$ . For positive bias, particle losses in the scrape-off layer are reduced while, in the main plasma, they are strongly increased. When the applied voltage goes from positive to negative, the particle losses are strongly reduced inside the limiter and increased in the scrape-off layer, leading to flatter edge density profiles.

#### 2.4.2.4. Electrode biasing

For electrode bias the changes in the plasma parameters are much more significant. For positive bias an increase ( $\sim 100\%$ ) in the line average plasma density is observed, which leads to a significant increase in particle confinement. The edge parameters, measured by the array of probes, are also strongly modified in the region between the electrode and the limiter.

Figure 2.11 shows a typical discharge with alternating electrode bias. The time evolution of the plasma current and temperature is very similar to that observed in limiter experiments. However, the electrode bias effects on the density and particle confinement are much larger than with limiter bias. For large positive applied voltage,  $V > 100$  V, a substantial increase ( $\sim 100\%$ ) in the average plasma density is observed, without significant changes in the edge density, leading to steeper profiles.

These results are corroborated by the Heavy Ion Beam diagnostic data, which shows steeper  $n_e\sigma_{\text{eff}}$  profiles for positive bias when compared with negative bias, particularly at the plasma edge. Although the  $H_\alpha$  radiation increases, the ratio  $n_e/H_\alpha$  also rises significantly ( $< 40\%$ ) indicating an improvement in gross particle confinement.

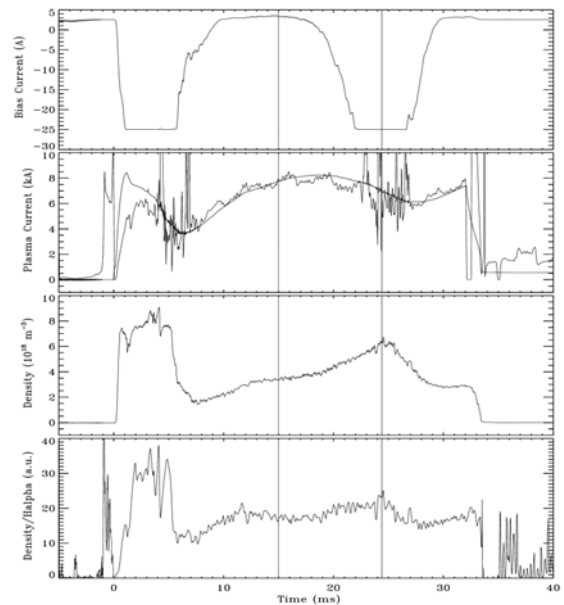


Figure 2.11 - Time evolution of the main plasma parameters for a discharge with EB

Figure 2.12 presents the time evolution of bias current together with the line average density,  $I_{\text{sat}}$ ,  $V_f$  and the cross field turbulent flux, for five discharges, corresponding to different radial probe positions. The floating potential near the electrode follows the applied voltage while close to the limiter the opposite behaviour is observed. The  $V_f$  profile is strongly modified by electrode bias. For  $V_{\text{bias}} < 80$  V,  $V_f$  is a monotonously decreasing function of the probe penetration into the plasma, (a-r), while for  $V_{\text{bias}} > 80$  V a clear inversion is observed.

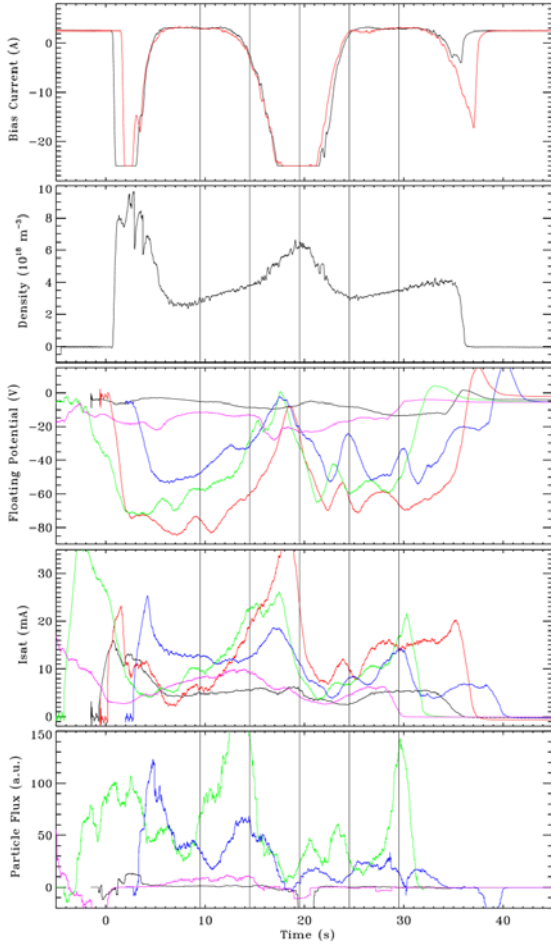


Figure 2.12 – Time evolution of the edge plasma parameters for EB

Figure 2.13 shows the radial profiles of  $V_f$ ,  $V_p$  and  $I_{sat}$  at different applied voltages taken from Figure 2.10. The plasma potential profile is very flat for negative and zero applied voltage, while for positive bias a large electric field is observed (values of  $E_r$  larger than 8 kV/m are observed). This suggests that EB creates a region with strong  $E \times B$  velocity shear inside the limiter, which may explain the improvement in particle confinement observed during that period.

Although the average density increases strongly up to  $t=19$  ms,  $I_{sat}$  at the limiter position is observed to decrease from  $t=14.5$  ms. This behaviour seems to propagate inwards; probes at smaller radius observe this reduction later, leading to progressively steeper profiles. In opposition, the turbulent transport is reduced strongly in the whole edge simultaneously.

The plasma average density is only strongly modified for  $V_{bias} > \approx 50$  V ( $t=16$  ms), suggesting that confinement modifications require a biasing voltage of that order. The modification in  $\langle n_e \rangle$  is preceded by the reduction in turbulent transport and  $I_{sat}$  at  $r=a$  ( $t=14.5$ ) and by a significant modification on  $V_p$  profile.

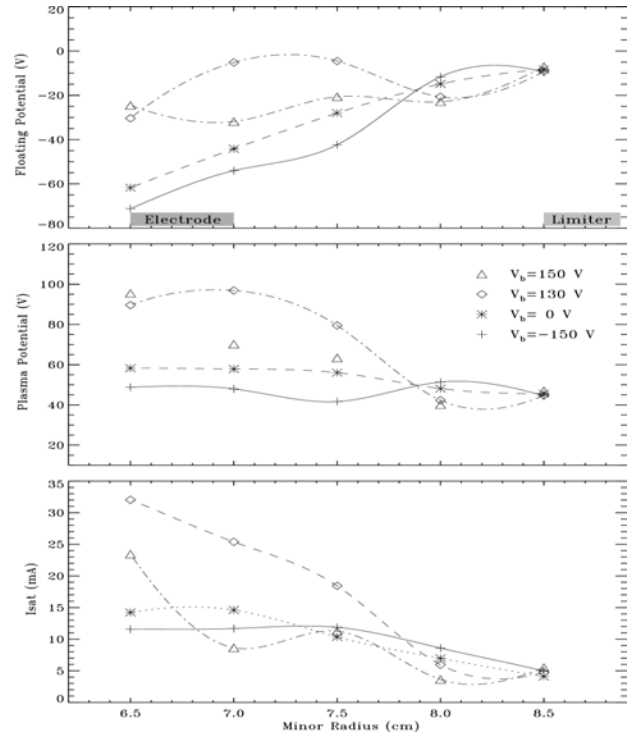


Figure 2.13 – Edge parameters radial profiles for a discharge with EB

The turbulent particle transport has been also computed from the probe data. Turbulent transport analysis indicates that for positive bias edge transport is strongly reduced leading to the observed steep profiles at the edge. The spectrogram of the particle flux due to fluctuations is also modified. It is broadband (10-100 kHz) for negative applied voltages while for positive bias the spectrum is dominated by frequencies between 20 and 40 kHz.

#### 2.4.2.5. Conclusions

The results presented above show that both limiter and electrode bias can modify the plasma behaviour, however, EB introduces larger alterations in the plasma parameters. The stronger modification in  $V_p$  observed for EB results in larger electric fields and consequently larger alterations in confinement. As expected, electrode bias is more efficient than limiter

biasing in modifying the radial electric field and confinement. Thresholds for confinement and stability modification usually require a biasing voltage in excess of 3-4  $kT_e/e$ .

A clear improvement in confinement is observed for positive bias with EB. A good correlation between confinement modifications and ExB shear has been found. In these bias experiments a radial electric field can be imposed in a controlled fashion and the issue of causality between  $E_r$  and confinement investigated in detail. It was clearly shown that modifications in confinement originate at the edge plasma as a consequence of the modifications in the radial electric field.

#### 2.4.3. Measurements of plasma potential fluctuations in the edge region

This section contains some measurements of the plasma potential ( $\Phi_{pl}$ ) and especially of its fluctuations, using electron-emissive probes. This diagnostic method is based on the fact that the electron emission current of such a probe is able to compensate temperature variations and electron drifts, which lead to erroneous results with the conventional cold probes.

An array of three emissive probes has been mounted in one of the radial flanges of ISTTOK. Each probe consists of an  $Al_2O_3$  tube of 2,8 mm outer diameter with four bores of 0,5 mm diam. each. Through two opposite bores, a 0,2 mm diam. tungsten wire is inserted so that a loop of about 5 mm length is formed. A current up to 7,2 A is needed to heat one emissive probe sufficiently. The three probes are situated on the same poloidal meridian, but on different poloidal positions. The probe tips are on different minor radii  $r_1 = 8,6$  cm,  $r_2 = 8,9$  cm and  $r_3 = 9,2$  cm. Thus all three probes are outside the last closed flux surface.

In order to make sensible measurements of the plasma potential an electron emission current of up to about 120 mA is necessary. Then the floating potentials of the emissive probes show  $\Phi_{pl}(r,t)$  on the three different radii. The plasma potential  $\Phi_{pl}(r_{1-3},t)$  were registered for various conditions allowing to obtain a rough radial profile of the plasma potential, showing also the temporal evolution during each shot. The power spectrum of the fluctuations were also calculated, which for  $100 \text{ Hz} < f < 60 \text{ kHz}$  is proportional to  $f^{-\alpha}$ , and  $\alpha$  turns out to be about 1,9. This can be a sign for the existence of flicker noise in the edge region, which is usually considered as a

proof for self-organised criticality of the density in the edge region.

#### 2.4.4. Transport modelling and numerical reconstruction of the runaway process

High values of the longitudinal electric field  $E_0 = V_{loop}/2\pi R_0 > 2-3 \text{ V/m}$  (Figure 2.14) provide the break down of the working gas and the creation of the plasma with a line-averaged density up to  $\langle n_e \rangle = (7-10) \cdot 10^{18} \text{ m}^{-3}$ . This density corresponds to a fairly complete ionisation of neutral hydrogen in a vacuum chamber at  $p_0 = (1-1.5) \cdot 10^{-4} \text{ torr}$ . Despite the fact that RA threshold at the discharge start-up inferred on the basis of the Townsend avalanche model:

$$E_0/p_0 > (2-2.5) \cdot 10^4 [\text{V} \cdot \text{m}^{-1} \cdot \text{torr}^{-1}] \quad (2.5)$$

was satisfied in our experiments, only a small number of shots entered into the RA regime from the beginning of the discharge.

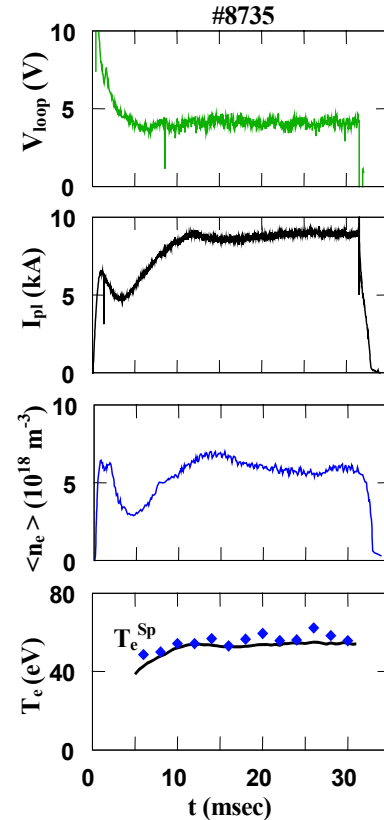


Figure 2.14 - Plasma parameters evolution in discharge #8735. The average electron temperature  $T_e^{Sp}$  (lower chart, diamonds) inferred from the measured plasma resistance is compared to the values of  $T_e$  calculated by the power-energy balance (solid line).

At  $n_e \gg n_a$  ( $n_a$  is the density of neutrals) the RA process is predominantly determined by the exponential term in expression for the classical RA production rate:

$$\lambda_{RA} \cong K(Z_e) * (E_e/E_e)^{3(Z+1)/16} n_e v_e \exp\{-E_e/4E_e / ((Z+1)E_e/E_e)^{1/2}\} \quad (2.6)$$

where  $e$  is the electron charge,  $\ln\Lambda$  is the Coulomb logarithm,  $Z_{eff}$  is the effective ion charge,

$$E_{CR} = e^3 \ln\Lambda n_e Z_{eff} / 4\pi\epsilon^2 T_e \quad (2.7)$$

is the Dreicer critical field and

$$v_e = 2.91 * 10^{-6} \ln\Lambda n_e Z_{eff} T_e^{-3/2} \quad (2.8)$$

is the electron collision frequency. The simple estimate shows, that at the plasma density  $\langle n_e \rangle \cong (7-10) * 10^{18} \text{ m}^{-3}$  achieved during the first 0.5-2 ms of the discharge, the RA generation is negligibly small. Nevertheless, further evolution of the majority of the ISTTOK discharges was characterized by the high probability of RA generation due to a significant decrease of the plasma density (Figure 2.15). In some cases, at the values of plasma current  $I_{pl} \cong 5-7 \text{ kA}$ , which usually were enough to sustain the plasma, the discharge was spontaneously terminated due to a sudden decrease of the ionisation rate and fast decay of the plasma density from the initially produced values. Analysis of the soft X-ray emission measured in the energy range 1-20 keV in some shots revealed noticeable increase of the emitted energy per X-ray quanta after the onset of the runaway regime.

In the quantitative reconstruction of the RA process the averaged values of the electron temperature inferred from the measured plasma resistance on the basis of Spitzer resistivity were used:

$$T_e^{Sp}(t) = [C_g * Z_{eff} f(Z_{eff}) * \ln\Lambda * I_{pl}(t) / V_{loop}(t)]^{2/3} \quad (2.9)$$

where  $C_g$  is a numeric coefficient, which includes the dependence on the geometrical parameters of the device, and  $f(Z_{eff})$  is the resistivity correction factor in impure plasmas. Spectroscopic measurements indicate the presence of the impurities, but it was not possible to evaluate accurately the values of  $Z_{eff}$ . A significant RA fraction in the total plasma current caused difficulty in the determination of the electron temperature using equation (2.9).

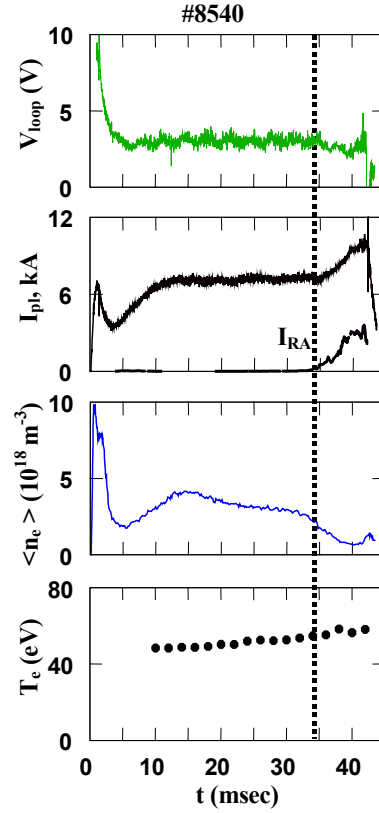


Figure 2.15 - Runaway generation in shot #8540. The onset of the runaway regime is marked by the vertical dotted line. Electron temperature  $T_e$  was evaluated by the power-energy balance taking into account the value of the RA current fraction ( $I_{RA}$ ).

To take into account the mutual dependence of  $T_e$ ,  $Z_{eff}$  and RA current, the evolution of the main plasma parameters, including electron temperature  $T_e(t)$  and generated RA current  $I_{RA}(t)$ , was simulated using calculations of the plasma transport and conventional issues of the RA theory. Equations of the power-energy balance for electrons, ions and atoms, as well as particle balance equations with characteristic confinement times inferred from the scaling of plasma confinement in tokamaks were used together with Ohm's law. The set of power-energy balance equations was completed by the equation of the electric circuit for a capacitor battery driven discharge in equivalent 'perfect transformer' scheme, and by the equation for the calculation of the RA current ( $I_{RA}$ ) in the 'continuous creation' model.

This calculation provided the adequate agreement between  $T_e(t)$  obtained from the power-energy

balance modelling and  $T_e^{Sp}(t)$  inferred from the measured plasma resistance. At the presence of runaways, this modelling enabled calculation of the RA current fraction ( $I_{RA}$ ) according to the actual values of  $T_e(t)$ , which, in turn, were updated according to the changes in the ratio between the resistive and RA currents and respective changes in macroscopic plasma parameters. This quantitative reconstruction of the RA process was done assuming that the loss of RA electrons generated at a certain time was negligibly small in comparison to the particle flux ( $\lambda_{RA}$ ) into the RA regime, and that this flux didn't significantly influence the discharge performance.

Strong oscillations of plasma parameters and subsequent strong changes in the plasma resistance due to the RA instability caused large uncertainties in calculations of  $T_e^{Sp}(t)$  directly from the measured  $I_{pl}(t)$  and  $V_{loop}(t)$ , and, therefore, in the evaluation of the RA current. In most cases, the calculations of the RA current yielded overestimated values for  $I_{RA}$  leading to a significant mismatch between the experimental  $I_{pl}(t)$ ,  $V_{loop}(t)$  and  $n_e(t)$  and the calculated ones.

To avoid the apparent systematic errors caused by the instability, the measured global plasma parameters were used in 0-D calculations of the plasma power-energy balance and equations for runaway-related analysis as 'stiff' boundary conditions, in which average  $T_e(t)$ ,  $n_{RA}(t)$  and  $I_{RA}(t)$  were calculated by iterations. The values of  $Z_{eff}$  were used as an iterative parameter to achieve the minimal deviations between the experimental  $I_{pl}(t)$  and  $V_{loop}(t)$  and those provided by the calculated values of  $T_e(t)$  and  $I_{RA}(t)$ .

Figure 2.16 presents results of the power-energy balance and RA current calculations at the presence of RA instability are presented. Calculated  $T_e(t)$  and  $I_{RA}(t)$  are shown together with the experimental traces of  $I_{pl}(t)$ ,  $V_{loop}(t)$  and  $n_e(t)$ . The electron temperature  $T_e^{Sp}(t)$  presented in these figures was inferred from the measured plasma resistance taking into account the values of calculated RA current.

In numerical reconstruction of the RA process and calculations of the electron temperature  $T_e(t)$ , the values of the confinement time of RA electrons ( $\tau_{RA}$ ) and their kinetic energy ( $W_{eRA}$ ) were used. These quantities ( $\tau_{RA}$  and  $W_{eRA}$ ) were obtained from the study of plasma parameters evolution in the presence of instability driven by the RA electrons.

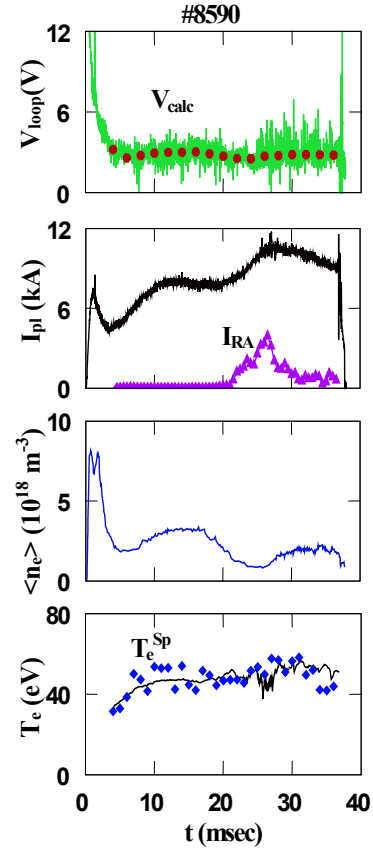


Figure 2.16 - RA instability in shot #8590. The instability onset (marked by vertical dotted line) is following the RA regime (started at  $t=20$  msec). Calculated resistive voltage  $V_{calc}$  (circles, upper chart) is compared to the experimental signal  $V_{loop}$ . The average electron temperature  $T_e^{Sp}$  (lower chart, diamonds) inferred from the measured plasma resistance taking into account RA current fraction ( $I_{RA}$ ) is presented in comparison to the values of  $T_e$  calculated by the power-energy balance (solid line).

Evaluated  $\tau_{RA}$  was verified by the comparison of the results of the integration of the electron motion under free acceleration with the results of calculations of  $T_e(t)$  and  $I_{RA}(t)$ , taking into account the 'stiffness' of the calculation boundaries. Obtained values of  $\tau_{RA} \leq 500 \mu s$  enabled to estimate the values of  $\gamma$  and the kinetic energy ( $W_{eRA}$ ) of the RA electrons at which the RA instability is detected in the discharges ( $W_{eRA} \sim 6-35$  keV, Figure 2.17). Results shown in Figure 2.18 adequately correspond to the conclusion of the theory of runaway instability that the higher the RA population presented in the discharge the lower the RA energy threshold required for the excitation of the RA instability.

Using the inferred range of values of the confinement time  $\tau_{RA}$ , it is possible to estimate roughly the corresponding averaged diffusion coefficient of the runaway electrons from the following expression:

$$D_{RA} \approx a_{pl}^2 / 5.6 \tau_{RA} \quad (2.10)$$

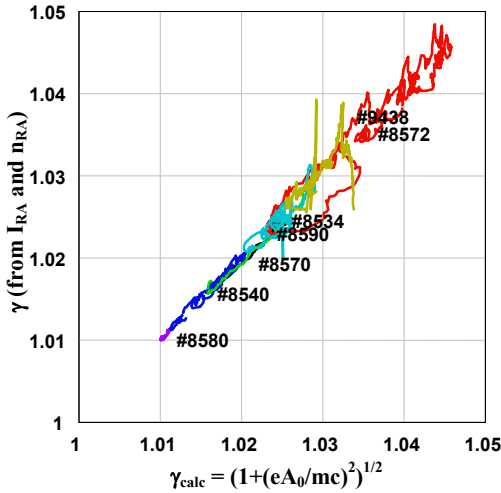


Figure 2.17 - Relativistic parameter  $\gamma = (1 - v_e^2/c^2)^{-1/2}$ , inferred from the calculated values of runaway current fraction  $I_{RA}$  and runaway electron density  $n_{RA}$ , plotted versus values of  $\gamma_{calc}$  obtained from the integration of the equation of motion

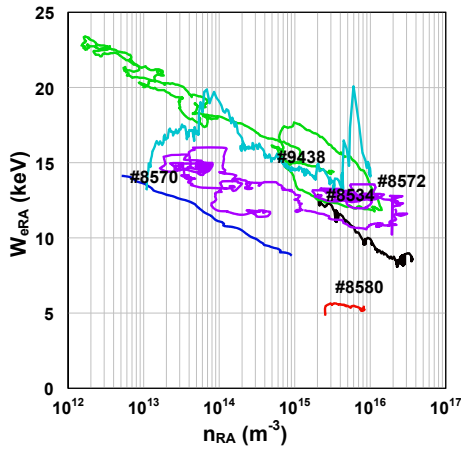


Figure 2.18 - The runaway electron energy  $W_{eRA}$  ( $W_{eRA} = 0.511 \text{ MeV} * (\gamma - 1)$ ) plotted as a function of the density of runaways at which the instability was detected in experiments.

Taking into account some uncertainties in determination of  $W_{eRA}$  we estimated the range of diffusion coefficient values as  $D_{RA} \approx 2-20 \text{ m}^2/\text{s}$ . These values of  $D_{RA}$  are adequately fitted to the results from other tokamak runaway experiments (Figure 2.19).

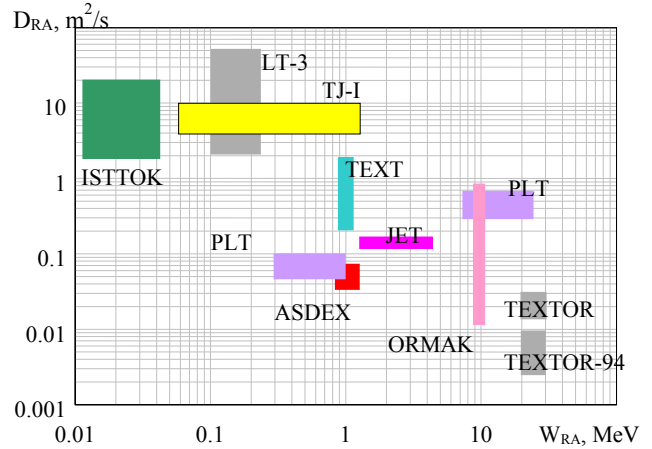


Figure 2.19 - Summary on results on diffusion of runaways in tokamaks. Main results are taken from [I. Entrop et al. Plasma Phys. and Contr. Fusion, 40(1998)1513] with inclusion of results of [L. Rodriguez-Rodrigo et al. Nuclear Fusion 34(1994)649] (TJ-I).